PHILOSOPHICAL
TRANSACTIONS A

royalsocietypublishing.org/journal/rsta

Research

Cite this article: Mohan D, Phanikumar G. 2019 Experimental and modelling studies for solidification of undercooled Ni–Fe–Si alloys. *Phil. Trans. R. Soc. A* **377**: 20180208.
http://dx.doi.org/10.1098/rsta.2018.0208

Accepted: 2 January 2019

One contribution of 17 to a theme issue 'Heterogeneous materials: metastable and non-ergodic internal structures'.

Subject Areas:
materials science

Keywords:
phase-field, dendrite theory, Ni–Fe–Si, undercooling, multi-component solidification

Author for correspondence:
Gandham Phanikumar
e-mail: gphani@iitm.ac.in

THE ROYAL SOCIETY
PUBLISHING

Experimental and modelling studies for solidification of undercooled Ni–Fe–Si alloys

Dasari Mohan and Gandham Phanikumar

Department of Metallurgical and Materials Engineering, Indian Institute of Technology Madras, Chennai 600 036, India

GP, 0000-0002-5198-317X

We present experimental results, analytical calculations and phase-field simulations for undercooled Ni–Fe–Si alloy system. Undercooling experiments are performed using flux encapsulation along with *in situ* measurement of recalescence speed using a high-speed camera followed by microstructural characterization. Dendrite growth calculations are performed using a modified Boettinger, Coriell and Trivedi theory to incorporate constitutional undercooling due to multiple segregating elements and a modified kinetic undercooling term. Phase-field simulations are performed using a multi-component phase-field model to generate dendrites in this alloy. High growth velocities are observed and the analytical calculations are in good agreement with experiments. The microstructure evolution from the phase-field simulations indicates that there is a difference in solute segregation during growth of dendrites.

This article is part of the theme issue 'Heterogeneous materials: metastable and non-ergodic internal structures'.

1. Introduction

Solidification of metallic systems has fundamental importance in manufacturing processes such as casting, welding and advanced techniques such as additive manufacturing [1]. Microstructure evolution during solidification in these processes decides the performance of a product. Integrated Computational Materials Engineering (ICME)-based platforms enable a faster and reliable product development cycle with the help of simulation tools along with experimental inputs [2]. Analysis of rapid solidification enables us to choose the appropriate processing conditions for phase selection in laser or electron beam-based additive manufacturing processes.

The industrially important alloys such as steels and superalloys are multi-component systems. Hence, it is essential to incorporate the solute interactions among all the components to understand the solidification behaviour of multi-component alloys. The measurement of undercooling using experiments can aid in the study of rapid solidification of multi-component systems [3]. The study of recalescence can be carried out by monitoring the thermal and spatial profiles during solidification in the undercooled melt [4].

The phase-field method is the most widely used technique for predicting microstructure evolution during phase transformations [5,6]. It is a diffuse interface approach, where an order parameter (ϕ) is used to describe the individual phases so that the explicit interface tracking is avoided. Phase-field models consider capillarity effects and can simulate complex microstructural features such as dendrites. Coupling of the thermodynamic database to the phase-field model during the simulations allows us to simulate the phase transformations in realistic multi-component alloys [7]. For quantitative results, phase-field models require smaller interface width, which demands finer grid spacing and time steps. Hence, these simulations require an enormous amount of computational resources and large memory for simulating realistic length scales [8,9].

Unlike the phase-field simulations, the calculations based on dendrite tip growth models are not computationally intensive. These models predict the dendrite tip velocity and radius for steady state dendrite growing at an undercooling below the equilibrium freezing temperature of the melt. The models are developed for operating state of the dendrite tip for pure materials, binary and multi-component alloys. The free dendrite growth theory for pure materials proposed by Lipton, Glicksmann & Kurz (LGK) [10] was limited to equilibrium interface at low undercoolings. Lipton, Kurz & Trivedi (LKT) [11] extended the LGK model for high growth rates. Interface kinetic effects to the LKT theory were incorporated by Boettinger, Coriell and Trivedi (BCT) [12]. Later, the effect of local non-equilibrium during rapid dendritic growth was introduced for binary alloys by Galenko & Danilov [13]. Further, models were also developed for ternary and multi-component systems for the solid–liquid interface growth rate [14,15]. In the above-mentioned models, the stability of the dendrite tip was given by marginal stability criteria [16] and recently the exact solution for the dendrite tip was obtained by microscopic solvability theory [17,18].

Bobadilla *et al.* [19] and Löser & Herlach [20] applied these theories for ternary alloys with an approximation of a linear phase diagram. The dendrite tip growth calculations for Fe–Cr–Ni ternary alloy were carried out with a linear phase diagram approach [19]. Experimental growth velocity of the α phase in the Fe-based quaternary alloy was understood only in terms of the binary alloy contributions [21]. A comprehensive study of dendrite growth using experiments, analytical calculations and phase-field simulations was reported for Ni–Al–Zr dilute ternary alloy [22].

There are very limited reports on the comprehensive study of dendrite tip growth including undercooling studies with experiments, analytical calculations and phase-field simulations for concentrated multi-component alloys. Hence, in this study, we have carried out undercooling experiments on Ni–Fe–Si alloy to study the growth rate kinetics of the primary solidifying phase. These experimental results were correlated with the modified BCT model by taking into account the solute interactions. These modifications were mainly focused on the constitutional undercooling and kinetic undercooling contributions. Phase-field simulations were carried out for the undercooled melt to analyse the microstructure evolution.

2. Phase-field method

The phase-field model uses an order parameter, $\phi(\boldsymbol{r}, t)$ for describing the phases. In this study, solid and liquid are represented by $\phi = 1$ and $\phi = 0$, respectively. In order to eliminate the chemical potential jump at the interface, we have used the anti-trapping multi-component phase-field model developed by Kim [23]. The brief details about the model used in this study are as follows.

Free energy functional, F of a system with $(n+1)$ components is given by

$$F = \int_V \left[\frac{\varepsilon_\phi^2}{2}|\nabla\phi|^2 + Wp(\phi) + h_p(\phi)f^S + [1-h_p(\phi)]f^L \right] \mathrm{d}V, \tag{2.1}$$

where ε_ϕ is the gradient energy coefficient, $p(\phi)$ is the double-well potential function, W is the height of the double well potential, $h_p(\phi)$ is the interpolation function for phase-field, f^S is the free energy density of the solid and f^L is the free energy density of the liquid. Phase transformations are studied by minimizing the above free energy functional. Phase-field evolution during solidification process is given by

$$\frac{1}{M_\phi}\frac{\partial\phi}{\partial t} = \varepsilon_\phi^2\nabla^2\phi - W\frac{\partial p(\phi)}{\partial\phi} - \frac{\partial h_p(\phi)}{\partial\phi}\left[f^S - f^L - \sum_{i=1}^{n}(c_i^S - c_i^L)\tilde{\mu}_i\right], \tag{2.2}$$

where M_ϕ is the phase-field mobility and $\tilde{\mu}_i$ is the chemical potential of ith component. The evolution of the concentration of ith component, c_i is given by

$$\frac{\partial c_i}{\partial t} = \nabla\cdot[1-h_d(\phi)]\sum_{j=1}^{n} D_{ij}^L \nabla c_j^L + \nabla\cdot j_{at}, \tag{2.3}$$

where $h_d(\phi)$ is the interpolation function for diffusion and D is the diffusivity. The anti-trapping term, j_{at} is given as

$$j_{at} = \frac{\varepsilon_\phi}{\sqrt{2W}}(c_i^L - c_i^S)\frac{\partial\phi}{\partial t}\frac{\nabla\phi}{|\nabla\phi|}. \tag{2.4}$$

Composition at the interface is given as the mixture of bulk compositions.

$$c_i = h_r(\phi)c_i^S + (1-h_r(\phi))c_i^L, \tag{2.5}$$

where $h_r(\phi)$ is the interpolation function for composition. The compositions c_i^L and c_i^S are restricted by the equal chemical potential condition at the interface

$$\frac{\partial f^S}{\partial c_i^S} = \frac{\partial f^L}{\partial c_i^L} \equiv \tilde{\mu}_i. \tag{2.6}$$

The composition of solid and liquid, c_i^L and c_i^S, is solved at every time step and grid point from equations (2.5) and (2.6) using the multi-dimensional Newton–Raphson method.

At a thin interface limit, the phase-field mobility and real interface mobility are given by the following relation:

$$\frac{1}{m} = \frac{1}{M_\phi}\frac{\sqrt{W}}{3\sqrt{2}\varepsilon} - a_2\frac{\varepsilon}{\sqrt{2W}}\zeta, \tag{2.7}$$

where a_2 is constant and given by $\int_0^1 (h(\phi)/\phi)\,\mathrm{d}\phi$ [23], with $h(\phi) = \phi^3(6\phi^2 - 15\phi + 10)$, a_2 is equal to $\frac{47}{60}$. To achieve an effective local equilibrium at the interface with infinite interface mobility, the phase-field mobility is given by

$$M_\phi = \frac{W}{3\varepsilon^2 a_2\zeta}. \tag{2.8}$$

This expression for the mobility is used in the phase-field evolution equation.

$$\zeta = (\Delta\boldsymbol{c}][\boldsymbol{A}^L][\boldsymbol{D}^L]^{-1}[\Delta\boldsymbol{c}), \tag{2.9}$$

where the matrix elements are represented as $(\Delta\boldsymbol{c}] = c_{iL}^e - c_{iS}^e$, $[\Delta\boldsymbol{c}) = (\Delta\boldsymbol{c}]^T$, $[\boldsymbol{A}^L] = \partial^2 f^L/\partial c_{iL}\partial c_{jL}$ and $[\boldsymbol{D}^L] = D_{ij}^L$.

Free energy of the liquid and solid in equation (2.1) is the Gibbs energy for phase-field simulations in real alloy systems. In order to simulate a realistic microstructure, one of the essential inputs to the phase-field models is thermodynamic information in the form of Gibbs energy of respective phases. These descriptions are obtained using the Calphad (CALculation of PHAse Diagram) method [24,25]. The Gibbs energy functions are available in the form of polynomials as a function of temperature (T), pressure (p) and composition.

The molar Gibbs energy, G_m, of a system has ideal, reference state and excess contributions at standard pressure which are given by

$$G_m = \sum_{i=1}^{n+1} c_i G_i^\circ + RT \sum_{i=1}^{n+1} c_i \ln c_i + G_m^{ex}, \tag{2.10}$$

where c_i is the composition of a component i, G_i° is the Gibbs energy of the pure component i and G_m^{ex} is the excess Gibbs energy. Excess Gibbs energy contribution is from binary, ternary and higher-order extrapolation terms is given by

$$G_m^{\text{ex}} = G_m^{\text{ex,bin}} + G_m^{\text{ex,tern}} + G_m^{\text{ex,hig}}. \tag{2.11}$$

For a ternary system, the contribution of constituent binary alloys is given by

$$G_m^{\text{ex,bin}} = \sum_{i=1}^{n} \sum_{j=i+1}^{n+1} c_i c_j L_{ij}, \tag{2.12}$$

$$L_{ij} = \sum_{\nu=0}^{l} (c_i - c_j)^\nu \cdot {}^{\nu}L_{ij} \tag{2.13}$$

and

$${}^{\nu}L_{ij} = {}^{\nu}a_{ij} + {}^{\nu}b_{ij}T. \tag{2.14}$$

The excess Gibbs energy for a ternary system is given by

$$G_m^{\text{ex,tern}} = \sum_{i=1}^{n-1} \sum_{j=i+1}^{n} \sum_{k=j+1}^{n+1} c_i c_j c_k L_{ijk} \tag{2.15}$$

and

$$L_{ijk} = \upsilon_i \cdot {}^{i}L_{ijk} + \upsilon_j \cdot {}^{j}L_{ijk} + \upsilon_k \cdot {}^{k}L_{ijk}, \tag{2.16}$$

where $\upsilon_i = c_i + (1 - c_i - c_j - c_k)/3$, $\upsilon_j = c_j + (1 - c_i - c_j - c_k)/3$, $\upsilon_k = c_k + (1 - c_i - c_j - c_k)/3$ and ${}^{\nu}L_{ijk} = {}^{\nu}a_{ijk} + {}^{\nu}b_{ijk}T$. ${}^{\nu}L_{ij}$ and ${}^{\nu}L_{ijk}$ are the Redlich–Kister parameters that are optimized using the Calphad approach.

3. Dendrite growth model

The total melt or bath undercooling (ΔT) of an alloy is the difference between the equilibrium liquidus temperature (T_L) and the temperature at dendrite tip. According to Boettinger *et al.* [12], the various contributions to ΔT are given as

$$\Delta T = \Delta T_t + \Delta T_r + \Delta T_c + \Delta T_k, \tag{3.1}$$

where ΔT_t is the thermal undercooling, ΔT_r is the Gibbs–Thomson undercooling due to the curvature of the dendrite tip, ΔT_c is the constitutional undercooling and ΔT_k kinetic undercooling describes the deviations from local equilibrium. These contributions can be calculated using the following relations. The thermal undercooling is given by [26]

$$\Delta T_t = \frac{\Delta H_f}{C_p^L} \, \text{Iv}(\text{Pe}_t) = T_Q \, \text{Iv}(\text{Pe}_t), \tag{3.2}$$

where C_p^l is the specific heat of the undercooled liquid, ΔH_f is the enthalpy of fusion, T_Q is hypercooling, $\text{Iv}(\text{Pe}_t)$ is the Ivantsov function and Pe_t is the thermal Peclet number which is given by

$$\mathrm{Pe}_t = \frac{VR}{2a}, \tag{3.3}$$

where V is the dendrite growth velocity, R is the dendrite tip radius and a is the thermal diffusivity. The undercooling due to curvature is given as [11]

$$\Delta T_r = 2\frac{\varGamma}{R}, \tag{3.4}$$

where $\varGamma$ is the Gibbs–Thomson coefficient, which is given as

$$\varGamma = \frac{\sigma_0}{\Delta S_f}, \tag{3.5}$$

σ_0 is the solid–liquid interfacial energy and ΔS_f is the entropy of fusion.

Constitutional undercooling for multi-component alloys was defined by [27] and is given as

$$\Delta T_c = T_L(c_1^0, c_2^0, \dots, c_n^0) - T_L(c_1^{*L}, c_2^{*L}, \dots, c_n^{*L}), \tag{3.6}$$

where c_i^0 is the composition of ith solute in the liquid. The above description for constitutional undercooling takes care of nonlinear liquidus surface for multi-component systems provided the composition-dependent liquidus temperature is calculated from the thermodynamic databases. c_i^{*L} is the composition of ith solute in the liquid at the dendrite tip which is given by [28]

$$c_i^* = \frac{c_i^0}{1-(1-k_i)\mathrm{Iv}(\mathrm{Pe}_i)}, \tag{3.7}$$

where Pe_i is the chemical Peclet number which is given as

$$\mathrm{Pe}_i = \frac{VR}{2D_i}, \tag{3.8}$$

where D_i is the chemical diffusion coefficient. The velocity-dependent partition coefficient is given by [29]

$$k_i(V) = \frac{k_{E,i} + V/V_{DI_i}}{1 + V/V_{DI_i}}, \tag{3.9}$$

where $k_{E,i}$ is the equilibrium partition coefficient of component i and V_{DI_i} is the interface diffusion velocity for component i. The kinetic undercooling is given by

$$\Delta T_k = \frac{V}{\mu}, \tag{3.10}$$

where μ is the interfacial kinetic coefficient which is given as [30]

$$\mu = \frac{R_g T_L^2}{\Delta H_f V_0}, \tag{3.11}$$

V_0 is the velocity of sound and R_g is the universal gas constant.

Equation (3.1) has two variables dendrite growth velocity V and dendrite tip radius R. In order to solve for the V and R the additional required equation is obtained from the stability analysis [16,31,32]. The second equation required to solve V and R used in this study is given by [19,20]

$$R = \frac{\varGamma/\sigma^*}{\mathrm{Pe}_t T_Q(1-n) - \sum_{i=1}^{2} 2\mathrm{Pe}_i m_i c_i^*(1-k_i)(1+g_i)}, \tag{3.12}$$

$$n = \frac{1}{\sqrt{1 + \frac{1}{\sigma^* \mathrm{Pe}_t^2}}} \tag{3.13}$$

and

$$g_i = \frac{2k_i}{1 - 2k_i - \sqrt{1 + 1/(\sigma^* \mathrm{Pe}_i^2)}}, \tag{3.14}$$

where $\sigma^* = 1/4\pi^2$ is the stability constant. Equations (3.12) and (3.1) together allow the calculation of dendrite tip velocity and radius as a function of undercooling.

4. Experimental details

Ni–Fe–Si alloys with 30 at.% Fe and 10 at.% Si were prepared using vacuum arc melting with a non-consumable tungsten electrode. The pure elements (greater than 99.9%) were weighed and melted in Ar atmosphere. The samples were melted for six times and the cast buttons were flipped after each melting to get a homogeneous distribution of alloying elements. The as-cast samples were in the form of buttons that weighed around 20 gm. These samples were cut to required quantity using electrical discharge machining (EDM). The cut samples were polished to remove the oxide layer and used further for undercooling experiments.

The undercooling experiments were carried out using melt fluxing technique with B_2O_3 as the flux. The time–temperature profiles were captured using a two colour infrared pyrometer with an accuracy of ±5°C. The high-speed imaging of the solidification process was captured using a Photron® FASTCAM high-speed camera at 10^5 frames/second. The captured data were analysed by using Photron® FASTCAM Viewer software. Structural characterization for the as-cast and undercooled samples was done using X-ray diffraction (XRD) (PANalytical® X'pert Pro) with Cu-Kα ($\lambda = 0.154$ nm) radiation with a step size of 0.02°. The diffractograms were analysed using X'pert High Score software. The microstructural characterization for these samples was performed using optical microscopy (Leica Microsystems®, Germany) after polishing and etching with Marbles reagent (10 ml HCl + 10 ml H_2O + 2 gm $CuSO_4$). A scanning electron microscope (SEM) (FEI® Quanta 400, USA) with an operating voltage of 20 kV, fitted with an energy-dispersive spectroscopy (EDS) attachment was used for further microstructural characterization as well as elemental composition analysis.

5. Computational details

(a) Phase-field method

The phase-field model was implemented using C-programming language and Graphical Processing Units (GPU) were used for accelerating the simulations using OpenCL libraries (D Mohan, Phanikumar G 2018, unpublished work). The accuracy of the phase-field results depends on the choice of interface width η and grid size Δx. The value of η should be less than the dendrite tip radius. In the present calculations, the ratio η/R is always greater than 1/3 [33] and hence, $\eta/\Delta x = 10$ is chosen. A 2048 × 2048 domain size was used in these calculations. Non-dimensionalized governing equations were solved using Euler explicit scheme. The time step Δt used in these simulations was $(\Delta x)^2/(5D_{\mathrm{SiSi}})$, which is less than $(\Delta x)^2/(2D_{\mathrm{SiSi}})$ the stability condition for explicit scheme [34].

In this work, we have used Thermo-Calc software [35] to calculate the Gibbs energies using the Calphad method. The commercial database for superalloys in Thermo-Calc (TCNI8) is encrypted and, hence, it is not possible to get the parameters in the Gibbs energy functions to be given as input in the phase-field simulations. Hence, the application programming interface of Thermo-Calc, known as the TQ interface was used to get the Gibbs energy values for different phases as a function of composition at various temperatures. These values were fitted to a polynomial as shown in equation (5.1). This is performed to improve the computational efficiency of the program.

The material parameters used in the phase-field simulations are listed in table 1. To obtain a larger domain, the dendrite tip growth direction is rotated by 45° with respect to the coordinate axis for better visualization.

Table 1. Material parameters used in the phase-field simulations.

parameter	units	value	source
σ_0	(J m^{-2})	0.25	present work
D^L_{FeFe} at 1636 K	(m^2 s^{-1})	2.51×10^{-9}	MOBNI4
D^L_{FeSi} at 1636 K	(m^2 s^{-1})	2.38×10^{-9}	MOBNI4
D^L_{SiFe} at 1636 K	(m^2 s^{-1})	2.52×10^{-9}	MOBNI4
D^L_{SiSi} at 1636 K	(m^2 s^{-1})	1.31×10^{-8}	MOBNI4
capillary anisotropy (ϵ_c)	—	0.03	present work

Table 2. Material parameters used in the dendrite tip growth model.

parameter	units	value	source
hypercooling	K	117.15	TCNI8
thermal diffusivity	m^2 s^{-1}	1.8×10^{-6}	present work
Gibbs–Thomson coefficient Γ	Km	1.0×10^{-7}	present work
velocity of sound (V_0)	m s^{-1}	4900.0	present work
interface diffusion velocity of Ni	m s^{-1}	5.0	present work
interface diffusion velocity of Si	m s^{-1}	10.0	present work
diffusion coefficient of Ni	m^2 s^{-1}	5.19×10^{-9}	MOBNI4
diffusion coefficient of Si	m^2 s^{-1}	1.08×10^{-8}	MOBNI4
kinetic coefficient	K	1100.85	present work

(b) Dendrite tip growth model

The material parameters used in the dendrite tip velocity and radius calculations are listed in table 2. The material parameters such as hypercooling, diffusion coefficients for each components were obtained from thermodynamic and diffusion databases TCNI8 and MOBNI4, respectively, from Themo-Calc software. Partition coefficients for Ni, Fe and Si were calculated as a function of temperature using TCNI8. A linear interpolation was used to estimate the equilibrium partition coefficient at a given undercooling for calculating the dendrite tip velocity and radius.

The constitutional undercooling is expressed as a linear combination of constituent elements for dilute ternary alloys, $\Delta T_c = \sum_{i=1}^{n} \Delta T_{c_i}$ [19,20]. This method deviates for the concentrated alloys where the liquidus surface is curved [27]. In order to account for the nonlinearity of the liquidus surface that is normally present in concentrated alloys, equation (3.6) was used. No explicit formula was given for the constitutional undercooling in this equation. The composition at the dendrite tip was calculated using equation (3.7). The difference in liquidus temperature at c_i^* and c_i^0 can be calculated from the thermodynamic database. In this work, the liquidus surface as a function of composition was calculated beforehand. These numerical data were fitted to a polynomial given by equation (5.1). This expression was used for the calculation of liquidus temperature and liquidus slope.

The polynomial used for fitting the numerical data is as follows:

$$B = \sum_{i=0}^{n} \sum_{j=0}^{n} a_{i,j} x_1^i x_2^j, \qquad (5.1)$$

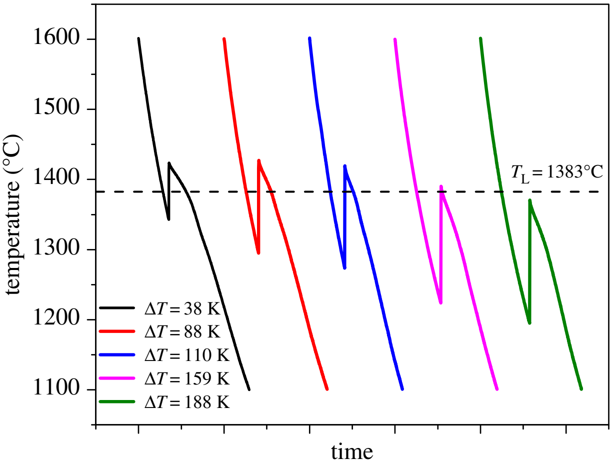

Figure 1. Time–temperature profiles at various undercoolings. Dotted line represents the liquidus temperature. (Online version in colour.)

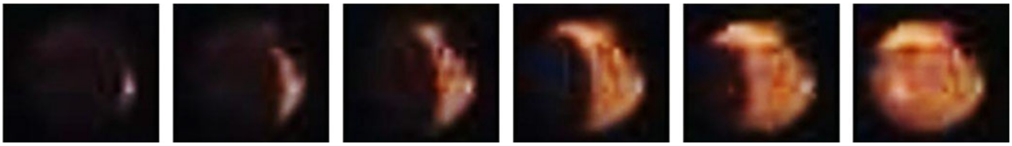

Figure 2. Snapshots of the video captured using high-speed camera during undercooling ($\Delta T = 159$ K). The diameter of the solidified sample is 5 mm from the last image. (Online version in colour.)

where B is composition-dependent material property such as G_m or T_L^{eq}, x_1 and x_2 are the mole fractions of component 1 and 2, respectively, $a_{i,j}$ is the fitting parameter and n is the order of the polynomial. $n = 5$ is being used for fitting in this work.

6. Results and discussion

(a) Experimental results

The time–temperature profiles of Ni–Fe–Si alloys with different undercooling are shown in figure 1. The liquidus temperature of the studied alloy is 1383°C taken from the TCNI8 database from Thermo-Calc. The undercooling temperature was calculated as the difference between the recalescence and liquidus temperatures. It is evident that there is no slope change after the undercooling, which confirms the solidification of a single phase. The series of images captured using the high-speed camera for the alloy that was undercooled to 159 K is shown in figure 2. In these images, the difference in the contrast is due to the evolution of latent heat during solidification. The dark region in the first image represents the initial melt and the bright region corresponds to the solid. This region starts from the edge and evolves into the melt as the solidification progresses. This can be observed from the series of snapshots provided from the high-speed video captured in our experiments.

X-ray diffractograms of the as-cast and undercooled samples are shown in figure 3. It can be observed that all the samples show a single phase with FCC crystal structure. These results are matching with the predictions from Thermo-Calc software that the primary solidifying phase is the single-phase FCC solid solution.

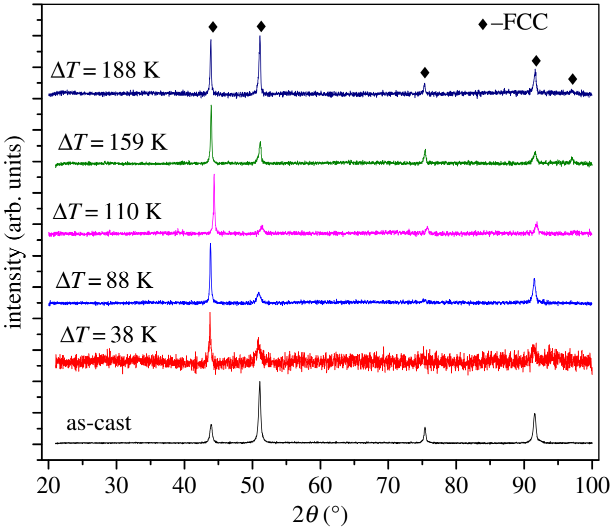

Figure 3. X-ray diffractograms of as-cast and undercooled Ni–Fe–Si alloys. (Online version in colour.)

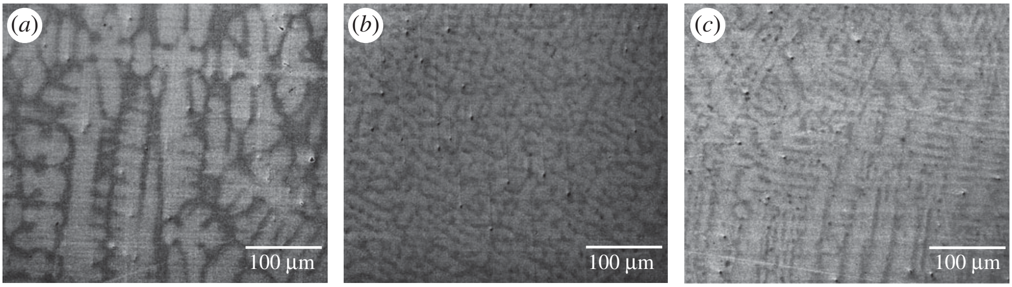

Figure 4. SEM-BSE micrographs of (*a*) as-cast, (*b*) $\Delta T = 38$ K and (*c*) $\Delta T = 88$ K undercooled alloys.

The back-scattered electron (BSE) images of the as-cast and $\Delta T = 38$ K, $\Delta T = 88$ K, $\Delta T = 110$ K samples captured using SEM are shown in figure 4. The dendritic microstructure was observed in the as-cast sample and no second phase was observed. Microstructure of the undercooled sample ($\Delta T = 38$ K) is fully dendritic. It shows a clear contrast between the dendritic and the interdendritic regions that indicates solute partitioning during solidification. With the increase in undercooling, reduction in the contrast between the dendritic and the interdendritic regions is observed, which is an indication of the onset of solute trapping.

It is evident that there is a dendrite to grain transition from the optical micrographs as shown in figure 5. The dendritic microstructure along with the grain boundary can be seen in the microstructure of samples with $\Delta T = 88$ K and $\Delta T = 110$ K. Fragmented dendrites can be seen for an undercooling of 159 K and the complete grain structure can be observed for the sample with highest undercooling (188 K) in this study. The formation of the grain structure with an increase in undercooling can be attributed to the increase in homogeneous nucleation sites within the alloy melt. This is followed by rapid solidification because of the large driving force for phase transformation.

The constitutional partition during solidification can be understood from the EDS spectrum. Figure 6 shows the EDS spectra for the sample with $\Delta T = 38$ K. The line at which the EDS scan was performed is marked in the SEM image. It can be inferred from the spectrum that there is enrichment of Si and Ni in the interdendritic region and that of Fe in dendrite. This is evident

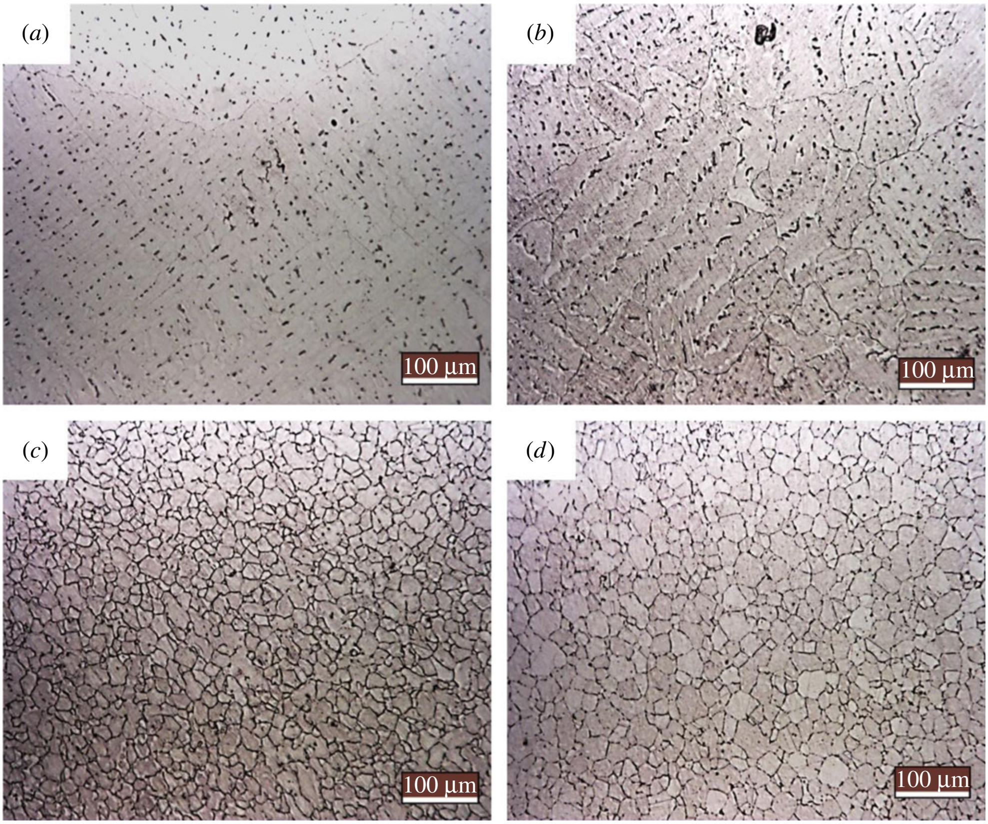

Figure 5. Optical micrographs of undercooled alloys (*a*) $\Delta T = 88$ K, (*b*) $\Delta T = 110$ K, (*c*) $\Delta T = 159$ K and (*d*) $\Delta T = 188$ K. (Online version in colour.)

from the phase diagram of the Ni–Fe–Si system where partition coefficient of the Ni and Si are less than 1 and that of Fe is greater than 1.

(b) Dendrite theory

The interface velocity measured using a high-speed camera along with the dendrite tip growth rate from theoretical calculations for various undercooling is shown in figure 7. The maximum growth velocity ($30.4 \pm 2.2\,\mathrm{m\,s^{-1}}$) was observed for the highest undercooling ($\Delta T = 188\,\mathrm{K}$) achieved in this work using experiments. A temperature-dependent kinetic coefficient of the form $\mu \cdot (p + q\Delta T)$ was used for analytical calculations [30]. The parameters $p = 1$ and $q = 0.092$ were obtained by fitting the dendrite tip velocity with experimental observations at higher undercooling. The underlying physics in dendrite tip evolution can be understood from the dendrite tip radius, composition and contributions to bath undercooling. Figure 8 shows the dendrite tip radius, fraction of undercooling, composition at dendrite tip and constitutional undercooling as a function of undercooling.

From figure 8*a*,*b*, it can be observed that for low undercooling ($\Delta T < 60\,\mathrm{K}$) a monotonous variation of dendrite tip radius, compositions of Fe and Si in solid and liquid. The decrease in R is due to the solutal interactions taking place at the interface. The composition of Fe at the interface decreases and composition of Si at the interface increases in the solid and liquid. As the undercooling changes, the compositions at the interface tries to adjust according to the local equilibrium which indicates a diffusion limited growth. The constitutional undercooling is dominant (greater than 75%) in this regime. The decrease in dendrite tip radius with undercooling

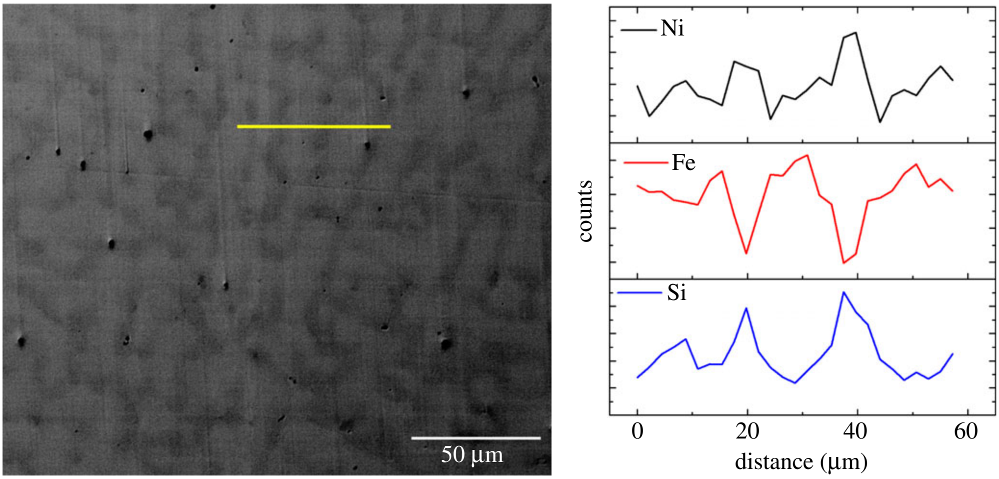

Figure 6. SEM-EDS mapping of Ni–Fe–Si alloy with $\Delta T = 38$ K undercooling. The line at which the EDS scan was performed is marked in the micrograph. (Online version in colour.)

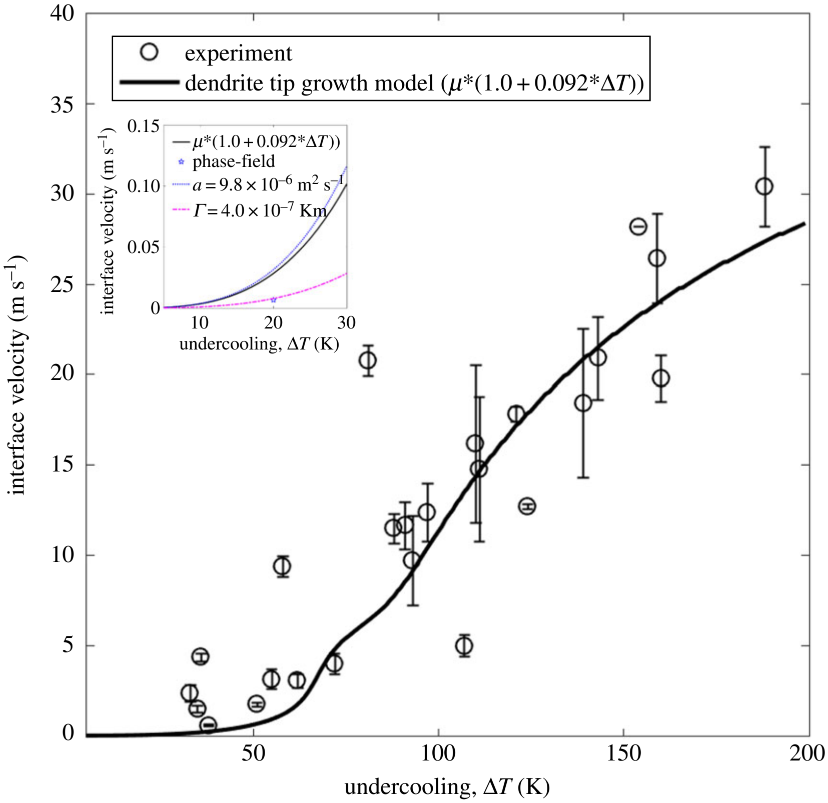

Figure 7. Experimentally measured interface velocity and calculated interface velocity using modified BCT theory at different undercooling for the primary solidifying phase. The inset shows the velocity from phase-field, the dependence of velocity on thermal conductivity and Gibbs–Thomson coefficient for the dendrite growth model. (Online version in colour.)

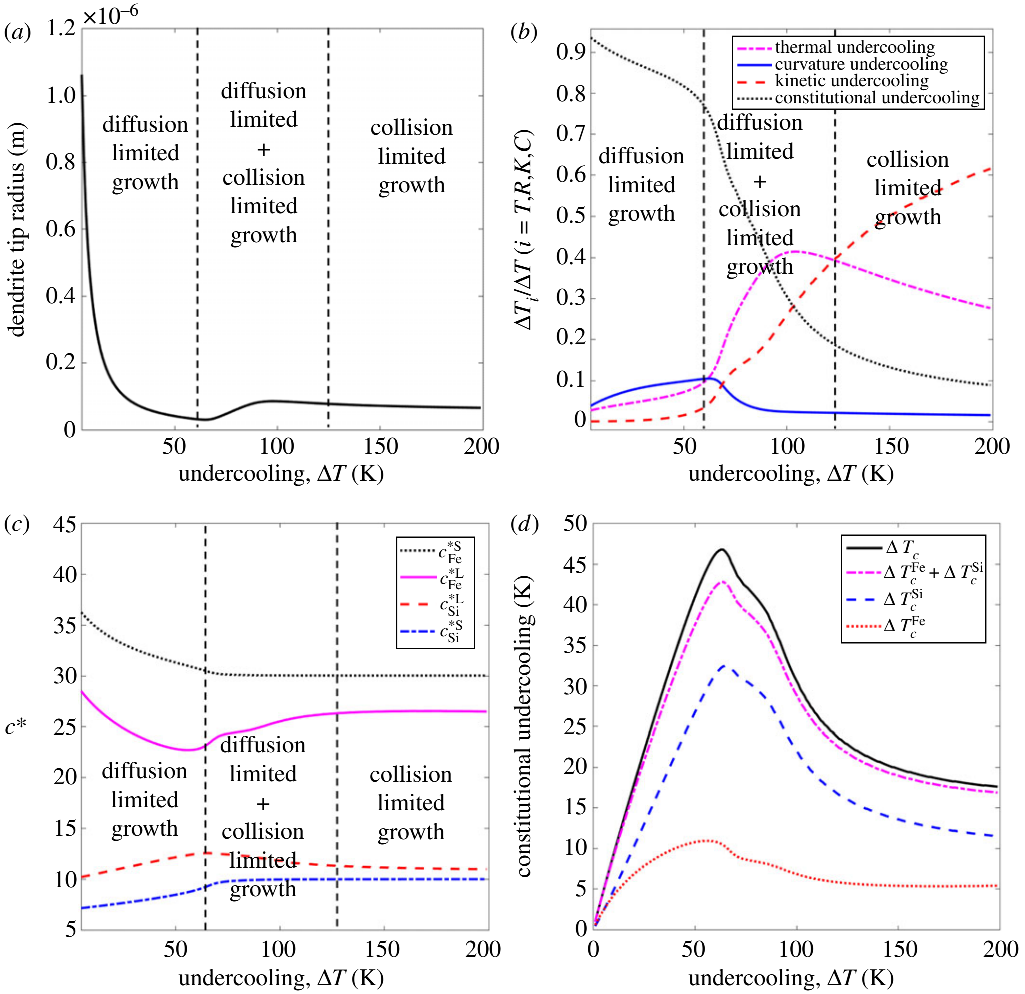

Figure 8. Evolution of (*a*) dendrite tip radius (*b*) fraction of undercoolings (*c*) compositions at the interface in solid and liquid and (*d*) solutal undercooling and its contributions with undercooling. Definitions for ΔT_c, $\Delta T_{\mathrm{Fe}} + \Delta T_{\mathrm{Si}}$, ΔT_{Fe} and ΔT_{Si} are given in the text. (Online version in colour.)

leads to an increase in the curvature undercooling contribution to the total undercooling as seen in figure 8*b*. For $\Delta T > 123\,\mathrm{K}$, variation in the dendrite tip is small which is evident from the near-constant profile of the interface composition of Fe and Si in solid and liquid. In this regime, kinetic undercooling is dominant, which indicates that the growth is governed by the interface attachment kinetics. It can be observed that at low and high undercooling, the variations of R, c^* are monotonous which indicates the preferred growth mode. However, for $60 < \Delta T < 123\,\mathrm{K}$, these variations are non-monotonous, indicating a mixed mode of growth. At intermediate undercooling, the solutal and curvature effects are the strongest. Also, the curvature effects are coupled strongly with multi-component solute diffusion field. Hence, we observe the nonlinearity in the growth rate and undercoolings is strong in this regime.

Figure 8*d* represents the constitutional undercooling as a function of total undercooling. The contributions of Fe and Si to ΔT_c are calculated using the following equations [27]:

$$\Delta T_c^{\mathrm{Fe}} = T_L^{\mathrm{eq}}(x_{\mathrm{Fe}}^0, x_{\mathrm{Si}}^0) - T_L^{\mathrm{eq}}(x_{\mathrm{Fe}}^{*L}, x_{\mathrm{Si}}^0) \qquad (6.1)$$

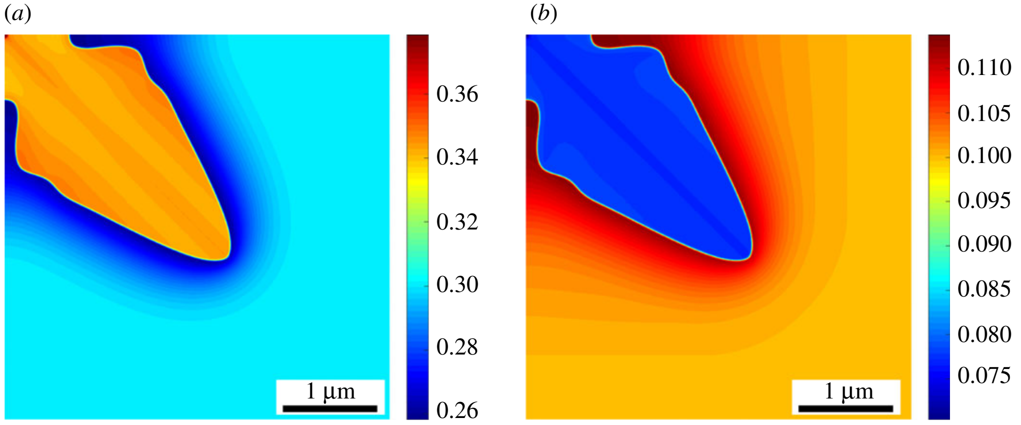

Figure 9. Dendrite morphology and composition profile for (*a*) Fe, (*b*) Si simulated using the phase-field method for $\Delta T =$ 20 K and growth duration of 46 µs. (Online version in colour.)

and

$$\Delta T_c^{\mathrm{Si}} = T_L^{\mathrm{eq}}(x_{\mathrm{Fe}}^0, x_{\mathrm{Si}}^0) - T_L^{\mathrm{eq}}(x_{\mathrm{Fe}}^{*L}, x_{\mathrm{Si}}^*). \tag{6.2}$$

From figure 8*d*, we can observe that the summation term underestimates the constitutional undercooling. As given in the works of Bobadilla *et al.* [19] and Löser & Herlach [20], if the linear addition of undercooling contributions is followed, the results will deviate significantly without considering the effects of solute interactions of the systems with nonlinear liquidus surface.

(c) Phase-field simulations

Figure 9 shows the composition map for Fe and Si simulated using the phase-field method at $\Delta T = 20\,\mathrm{K}$ for a growth duration of 46 µs. These results can be considered as representative simulations for low undercooling experiments. The dendrite tip growth direction is rotated by 45° with respect to the coordinate axis. The grid size and time step of the simulation are 2.0×10^{-9} m and 6.1×10^{-11} s, respectively. The calculated velocity of the dendrite tip from the phase-field simulation is $6.6 \times 10^{-3}\,\mathrm{m\,s^{-1}}$. For $\Delta T = 20\,\mathrm{K}$, the analytical model predicts the velocity of the dendrite tip to be $2.8 \times 10^{-2}\,\mathrm{m\,s^{-1}}$. This can be understood by performing a systematic study of the dependence of material parameters in both the models. From figure 9, it can be observed that Fe is enriched in the growing solid dendrite and Si is enriched in the liquid at the dendrite interface. This can be correlated with results of EDS which show enriched Si and depleted Fe in the interdendritic region (figure 6). The solute diffuse boundary of Si is longer when compared with Fe, which indicates that the solutal undercooling is dominated by Si. This can be inferred from figure 8*d*.

7. Conclusion

In this work, interface growth velocity and undercooling for Ni–Fe–Si alloys were measured using flux undercooling experiments. The structural and microstructural characterization confirms the formation of a single phase during solidification. The highest growth velocity achieved was $30.4 \pm 2.2\,\mathrm{m\,s^{-1}}$. The dendrite growth theory was used for analytical calculations from which three modes of dendrite growth were identified. The interaction of solutes leads to nonlinear behaviour of dendrite tip radius and velocity with respect to undercooling. This was achieved by incorporating a modified term for constitutional undercooling. The temperature-dependent kinetic coefficient indicates that the interface attachment dominates the growth of the dendrite. Phase-field simulations were carried out to study the spatial evolution of the microstructure. Si was found to have a longer solute boundary layer compared with Fe. Also, Fe is enriched in the solid phase and Si is enriched in the liquid phase.

Data accessibility. This article has no additional data.

Authors' contributions. This is a research work carried out by D.M. under the guidance of G.P. for a doctoral thesis. All authors read and approved the manuscript.

Competing interests. We declare we have no competing interests.

Funding. This work was not funded by any agency.

Acknowledgements. D.M. would like to acknowledge the help received from Rahul M. R. and B. Nithin for carrying out the experimental work. He would also like to thank R. Ramakrishnan for the technical discussions.

References

1. Ghosh S. 2018 Predictive modeling of solidification during laser additive manufacturing of nickel superalloys: recent developments, future directions. *Mater. Res. Express* **5**, 012001. (doi:10.1088/2053-1591/aaa04c)
2. Allison J, Cowles B, DeLoach J, Pollock TM, Spanos G. 2013 Integrated computational materials engineering (ICME): implementing ICME in the aerospace, automotive, and maritime industries. In *A study organized by the minerals, metals & materials society*, vol. 15086, pp. 9–10. Warrendale, PA: The Minerals, Metals & Materials Society.
3. Ruan Y, Mohajerani A, Dao M. 2016 Microstructural and mechanical-property manipulation through rapid dendrite growth and undercooling in an Fe-based multinary alloy. *Sci. Rep.* **6**, 31684. (doi:10.1038/srep31684)
4. Herlach DM. 2014 Non-equilibrium solidification of undercooled metallic melts. *Metals* **4**, 196–234. (doi:10.3390/met4020196)
5. Steinbach I. 2009 Phase-field models in materials science. *Model. Simul. Mater. Sci. Eng* **17**, 073001. (doi:10.1088/0965-0393/17/7/073001)
6. Boettinger WJ, Warren JA, Beckermann C, Karma A. 2002 Phase-field simulation of solidification. *Annu. Rev. Mater. Res.* **32**, 163–194. (doi:10.1146/annurev.matsci.32.101901.155803)
7. Steinbach I, Böttger B, Eiken J, Warnken N, Fries SG. 2007 CALPHAD and phase-field modeling: a successful liaison. *J. Phase Equilib. Diff.* **28**, 101–106. (doi:10.1007/s11669-006-9009-2)
8. Tennyson G, Karthik GM, Phanikumar G. 2015 MPI+ OpenCL implementation of a phase-field method incorporating CALPHAD description of Gibbs energies on heterogeneous computing platforms. *Comput. Phys. Commun.* **186**, 48–64. (doi:10.1016/j.cpc.2014.09.014)
9. Karma A, Wouter-Jan R. 1998 Quantitative phase-field modeling of dendritic growth in two and three dimensions. *Phys. Rev. E* **57**, 4323. (doi:10.1103/PhysRevE.57.4323)
10. Lipton J, Glicksman ME, Kurz W. 1984 Dendritic growth into undercooled alloy metals. *Mater. Sci. Eng.* **65**, 57–63. (doi:10.1016/0025-5416(84)90199-X)
11. Lipton J, Kurz W, Trivedi R. 1987 Rapid dendrite growth in undercooled alloys. *Acta Metall.* **35**, 957–964. (doi:10.1016/0001-6160(87)90174-X)
12. Boettinger WJ, Coriell SR, Trivedi R. 1988 Application of dendritic growth theory to the interpretation of rapid solidification microstructure. *Rapid Solidification Processing: Principles and Technology*, 13.
13. Galenko PK, Danilov DA. 1997 Local nonequilibrium effect on rapid dendritic growth in a binary alloy melt. *Phys. Lett. A* **235**, 271–280. (doi:10.1016/S0375-9601(97)00562-8)
14. Ludwig A, Pustal B, Herlach DM. 2001 General concept for a stability analysis of a planar interface under rapid solidification conditions in multi-component alloy systems. *Mater. Sci. Eng. A* **304**, 277–280. (doi:10.1016/S0921-5093(00)01451-9)
15. Alexandrov DV, Dubovoi GY, Malygin AP, Nizovtseva IG, Toropova LV. 2017 Solidification of ternary systems with a nonlinear phase diagram. *Russ. Metall.* **2017**, 127–135. (doi:10.1134/S0036029517020021)
16. Langer J, Müller-Krumbhaar H. 1978 Theory of dendritic growth—I. Elements of a stability analysis. *Acta Metall.* **26**, 1681–1687. (doi:10.1016/0001-6160(78)90078-0)

17. Alexandrov DV, Pinigin DA. 2013 Selection of stable growth conditions for the parabolic dendrite tip in crystallization of multicomponent melts. *Tech. Phys.* **58**, 309–315. (doi:10.1134/S106378421303002X)
18. Pelce P, Bensimon D. 1987 Theory of dendrite dynamics. *Nucl. Phys. B* **2**, 259–270. (doi:10.1016/0920-5632(87)90022-3)
19. Bobadilla M, Lacaze J, Lesoult G. 1988 Influence des conditions de solidification sur le déroulement de la solidification des aciers inoxydables austénitiques. *J. Cryst. Growth* **89**, 531–544. (doi:10.1016/0022-0248(88)90216-3)
20. Löser W, Herlach D. 1992 Theoretical treatment of the solidification of undercooled Fe–Cr–Ni melts. *Metall. Trans. A* **23**, 1585–1591. (doi:10.1007/BF02647340)
21. Ruan Y, Dai FP. 2012 Rapid dendrite growth subjected to multi-solute trapping in an undercooled Fe-based quaternary alloy. *Intermetallics* **25**, 80–85. (doi:10.1016/j.intermet.2012.02.017)
22. Galenko PK, Reutzel S, Herlach DM, Fries SG, Steinbach I, Apel M. 2009 Dendritic solidification in undercooled Ni–Zr–Al melts: experiments and modeling. *Acta Metall.* **57**, 6166–6175. (doi:10.1016/j.actamat.2009.08.043)
23. Kim SG. 2007 A phase-field model with antitrapping current for multicomponent alloys with arbitrary thermodynamic properties. *Acta Mater.* **55**, 4391–4399. (doi:10.1016/j.actamat.2007.04.004)
24. Saunders N, Miodownik AP. 1998 *CALPHAD (calculation of phase diagrams): a comprehensive guide*, vol. 1. Amsterdam, The Netherlands: Elsevier.
25. Lukas HL, Fries SG, Sundman B. 2007 *Computational thermodynamics: the Calphad method*. Cambridge, UK: Cambridge University Press.
26. Ivantsov GP. 1947 Temperature field around a spherical, cylindrical, and needle-shaped crystal, growing in a pre-cooled melt. *Dokl. Akad. Nauk SSR.* **58**, 567–569.
27. Wang K, Wang H, Liu F, Zhai H. 2013 Modeling dendrite growth in undercooled concentrated multi-component alloys. *Acta Mater.* **61**, 4254–4265. (doi:10.1016/j.actamat.2013.03.051)
28. Ivantsov GP. 1952 On a growth of spherical and needle-like crystals of a binary alloy. *Dokl. Akad. Nauk SSSR* **83**, 573–575.
29. Aziz MJ. 1982 Model for solute redistribution during rapid solidification. *J. Appl. Phys.* **53**, 1158–1168. (doi:10.1063/1.329867)
30. Phanikumar G, Biswas K, Funke O, Holland-Moritz D, Herlach DM, Chattopadhyay K. 2005 Solidification of undercooled peritectic Fe–Ge alloy. *Acta Mater.* **53**, 3591–3600. (doi:10.1016/j.actamat.2005.03.053)
31. Alexandrov D, Danilov D, Galenko P. 2016 Selection criterion of a stable dendrite growth in rapid solidification. *Int. J. Heat Mass Transfer* **101**, 789–799. (doi:10.1016/j.ijheatmasstransfer.2016.05.085)
32. Galenko P. 2007 Solute trapping and diffusionless solidification in a binary system. *Phys. Rev. E* **76**, 031606. (doi:10.1103/PhysRevE.76.031606)
33. Apel M, Steinbach I. 2008 Dendritic solidification in the diffuse regime and under the influence of buoyancy-driven melt convection. In *Phase transformations in multicomponent melts*, pp. 373–385. Weinheim, Germany: Wiley-VCH Verlag GmbH & Co.
34. Cha P-R, Yeon D-H, Yoon J-K. 2001 A phase field model for isothermal solidification of multicomponent alloys. *Acta Metall.* **49**, 3295–3307. (doi:10.1016/S1359-6454(01)00184-7)
35. Sundman B, Jansson B, Andersson JO. 1985 The Thermo-Calc databank system. *Calphad* **9**, 153–190. (doi:10.1016/0364-5916(85)90021-5)